Available online at www.sciencedirect.com

SciVerse ScienceDirect

Acta Materialia 61 (2013) 4053–4065

Acta MATERIALIA

www.elsevier.com/locate/actamat

Simulation of solid deformation during solidification: Compression of a single dendrite

M. Yamaguchi, C. Beckermann *

Department of Mechanical and Industrial Engineering, University of Iowa, Iowa City, IA 52242, USA

Received 27 December 2012; accepted 20 March 2013
Available online 22 April 2013

Abstract

A method is developed to numerically simulate coupled solidification and deformation of dendrites. Dendritic solidification is modeled using the phase-field method. The elasto-viscoplastic deformation of the growing solid is computed using the material point method. The stress analysis assumes a sharp and stress free solid–liquid interface, with the zero contour line of the phase field used to identify the interface. The deformation-induced flow in the liquid is approximated through a zero-gradient extension of the deformation velocities in the solid. Changes in the crystallographic orientation angle and advection of the phase and temperature fields due to solid deformation are all accounted for. Numerous tests are performed to validate the various numerical procedures. The full model is then applied to simulate in two dimensions the compression of a single dendrite of a pure substance growing in an undercooled melt. The development of complex stress and strain distributions is observed. The deformations result in variations in the crystallographic orientation angle within the dendrite that, in turn, affect the subsequent solidification behavior. The modeling of the deformation of polycrystalline solidifying structures, including the formation of grain boundaries, is described in a companion paper.

Keywords: Dendritic growth; Viscoplastic deformation; Phase-field method; Material point method

1. Introduction

Deformation of the solid is a common occurrence during metal casting processes [1,2]. Often the solid deforms simply due to thermal stresses, but sometimes the deformation is caused by external forces, for example through the rolls in continuous casting, mold wall movement, or an applied pressure. When the casting is still solidifying, the deformations can extend into the semi-solid mushy zone. This mushy zone is typically composed of solid dendrites surrounded by liquid. Deformation of the mush can lead to numerous defects in a solidified casting, including hot tears, macrosegregation and porosity. Therefore, understanding the mechanical behavior of mush is of great interest for advancing casting simulations incorporating a stress analysis and, ultimately, for preventing defects in castings [3].

The overall goal of the present study is to develop a numerical method for simulating the deformation of a solidifying mush on the scale of the evolving microstructure. Such direct numerical simulations may lead to improved constitutive models for use in macroscopic stress simulations. Mush deformation is a complex process involving multiple physical phenomena: solidification and formation of bridges or grain boundaries between dendrites, large inelastic solid deformation with contacts, liquid flow, etc. Simulating all of these processes simultaneously would be a very challenging task. A few researchers have developed methods to investigate the mechanical behavior of mush. Phillion et al. [4] and Fuloria and Lee [5] calculated inelastic deformation of multi-grain and dendritic microstructures, respectively, without considering solidification. Uehara et al. [6] performed thermal stress simulations in a confined solidifying microstructure. Fully

* Corresponding author. Tel.: +1 319 335 5681; fax: +1 319 335 5669.
E-mail address: becker@engineering.uiowa.edu (C. Beckermann).

1359-6454/$36.00
http://dx.doi.org/10.1016/j.actamat.2013.03.030

coupled solidification and deformation simulations of dendritic microstructures have not been performed in the past. The coupling of the solidification and deformation calculations is important not only because the deformations are a function of the morphology of the evolving solid, but also because the solidification patterns are affected by the deformations. In order to simplify the problem, we focus in the present study on dendritic solidification and solid deformation of a pure substance in two dimensions. Stresses that are exerted by the liquid on the solid are neglected. This assumption is realistic when the liquid can "drain" freely. In fact, the flow of the liquid is not modeled at all. Transformation stresses/strains, stress-induced phase transformations, and heat generation due to inelastic deformation are not considered. These assumptions are all appropriate for a slowly deforming mush. All material properties are assumed to be constant, and the thermophysical properties of the solid and liquid are assumed to be equal.

The simulation of dendritic solidification with large solid deformations necessitates numerous choices regarding the models to be used and the numerical methods to be employed. The phase-field method [7,8] is used in the present study to simulate solidification. Since it employs a diffuse interface concept, it is especially well suited for handling morphological changes and singularities, such as those caused by portions of a dendrite impinging on one another. Such wetting and bridging phenomena are not well handled by traditional sharp interface approaches. In addition, phase-field methods are available to simulate solidification of multiple crystals while accounting for their individual crystallographic orientations and the formation of grain boundaries [9]. The main new feature of the present phase-field calculations is that due to the deformation of the solid, the crystallographic orientation angle is no longer uniform within a single dendrite and continuously evolves. Furthermore, the phase-field and the temperature field are advected by the deformation velocity. The stress model for simulating the elasto-viscoplastic deformation of the solid assumes that the solid–liquid interface is sharp. The zero contour line of the phase field is used to identify the interface. The stress model is only solved in the solid and the solid–liquid interface is taken as stress free. The numerical method employed in the solution of the stress model needs to be able to handle large strains, self-contact and impingement of solid. Particle methods or meshless methods are attractive for this purpose, because they do not suffer from the mesh collapse or entanglement problems typical of Lagrangian finite-element methods (FEMs). In the present study, the material point method [10] is selected. The main feature of this method is that is uses, as in a particle method, a Lagrangian description for the motion of material points, and a fixed Eulerian background mesh for solving the equation of motion. The latter feature makes the material point method well suited for coupling with the (Eulerian) phase-field method.

The present paper is limited to the simulation of the coupled solidification and deformation of a single dendrite. This simplification is made in order to allow for detailed testing and validation of the methods employed. Several examples are presented that illustrate the complex physical phenomena involved. A companion paper [11] then extends the present method to consider multiple dendrites and grain boundaries.

2. Models and numerical procedures

2.1. Phase-field method for dendritic solidification in the presence of solid deformation

The standard phase-field model of Karma and Rappel [12] is used to simulate dendritic solidification of a pure substance from an undercooled liquid melt. Let ϕ denote the phase field, where $\phi = \pm 1$ refers to the bulk solid and liquid phases, respectively. The anisotropic form of the two-dimensional phase-field evolution equation is given by:

$$\tau_\phi(\alpha)\left(\frac{\partial \phi}{\partial t} + \boldsymbol{v}\cdot\nabla\phi\right) = \nabla\cdot\left[W^2(\alpha)\nabla\phi\right] - \frac{\partial f(\phi,\lambda\theta)}{\partial\phi} + \frac{\partial}{\partial x}\left[|\nabla\phi|^2 W(\alpha)\frac{\partial W(\alpha)}{\partial \phi_x}\right] + \frac{\partial}{\partial y}\left[|\nabla\phi|^2 W(\alpha)\frac{\partial W(\alpha)}{\partial \phi_y}\right], \quad (1)$$

where $\tau_\phi(\alpha) = \tau_0\xi^2(\alpha)$ and $W(\alpha) = {}_0\xi(\alpha)$ are orientation-dependent relaxation time and diffuse interface thickness parameters, respectively, in which α is the (crystallographic orientation) angle between the interface normal and the crystal axes. The usual 4-fold crystalline anisotropy function $\xi = 1 + \varepsilon\cos(4\alpha)$ is used, where ε is the anisotropy strength of the surface energy. The phenomenological bulk free energy function is given by $f(\phi,\lambda\theta) = q(\phi) + \lambda\theta p(\phi)$, in which $q(\phi) = -\phi^2/2 + \phi^4/4$ is a double-well function and $p(\phi) = \phi - 2\phi^3/3 + \phi^5/5$ is an odd function. The dimensionless temperature is given by $\theta = (T - T_m)/(L/c_p)$, in which T, T_m, L and c_p are the temperature, melting point, latent heat and specific heat, respectively. The coupling constant, λ, and the relaxation time, τ_0, are chosen in accordance with the thin-interface analysis of Karma and Rappel [12] in order to model kinetics-free growth. The parameter W_0 has to be reduced until a converged solution that is independent of the diffuse interface thickness is obtained. The temperature field is obtained from the following heat equation:

$$\frac{\partial\theta}{\partial t} + \boldsymbol{v}\cdot\nabla\theta = D\nabla^2\theta + \frac{1}{2}\left(\frac{\partial\phi}{\partial t} + \boldsymbol{v}\cdot\nabla\phi\right), \quad (2)$$

where D is the thermal diffusivity. All other details can be found in the original Ref. [12].

The terms in Eqs. (1) and (2) involving the velocity vector, $\boldsymbol{v}$, account for advection of the phase field and the temperature field. Since Eqs. (1) and (2) are solved over the entire computational domain, the velocity field must be known everywhere. The deformation velocity in the solid

($\phi > 0$) is given by the stress model (see below). However, since the flow in the liquid ($\phi < 0$) is not modeled in the present study (see Introduction), a liquid velocity field must be prescribed. Setting the velocity in the liquid phase to zero would not be appropriate, because it would lead to an unrealistic velocity variation inside of the diffuse interface and no advection of the temperature field in the liquid. Instead, it is assumed that the liquid velocity is given by a zero-gradient extension of the solid velocity in the direction normal to the solid–liquid interface, i.e. the liquid at any point in space and time has the same velocity as the closest solid. The PDE-based scheme of Gibou et al. [13] is used to perform the velocity extension. The inverse of the phase field is used as a signed-distance (level set) function [14], and the PDE-based reinitialization scheme of Osher and Fedkiw [15] is employed to maintain an accurate signed-distance function over the entire computational domain. Due to the continuity of the solid and liquid velocities at the solid–liquid interface (for equal densities), the present approach can be expected to yield realistic liquid velocities near the interface. However, the liquid velocity field away from the interface can be affected by many factors aside from the solid deformation. Nonetheless, a full solution of the Navier–Stokes equations for the liquid is outside the scope of the present study.

The solid deformation also changes the crystallographic orientation angle, α. The angle can evolve in time due to advection and rotation, such that the following evolution equation can be written:

$$\frac{\partial \alpha}{\partial t} + \boldsymbol{v} \cdot \nabla \alpha = \nabla \times \boldsymbol{v}. \tag{3}$$

The term on the right-hand side of Eq. (3) is needed so that for a spatially uniform angle, i.e. for an undeformed crystal where $\nabla \alpha = 0$, rigid-body rotational movement of the solid still results in angle changes. Since the orientation angle is only defined for the solid, but Eq. (3) is solved over the entire domain, the orientation angle is numerically extended into the liquid using again the extension scheme of Gibou et al. [13]. While there is no physical meaning associated with this procedure, it results in the liquid having an orientation angle equal to the one of the closest solid.

The above model neglects the formation of a grain boundary when there is a crystallographic orientation angle mismatch between two interacting portions of a deformed dendrite. In other words, the model is limited to situations where solid regions with different orientations do not impinge on or grow into each other. As already mentioned, the companion paper [11] includes these interactions via a polycrystalline phase-field model [9].

The above equations are solved numerically on a fixed Eulerian mesh using a standard explicit finite-difference discretization. The fractional step or operator splitting approach [16] is employed to allow for different time steps to be used for the advection and diffusion terms. Special care needs to be taken in the numerical treatment of the advection terms, i.e. those involving $\boldsymbol{v} \cdot \nabla$, especially for the phase-field [17]. In the present study, the CIP method [18] is adopted for this purpose. It is a third-order scheme that prevents the numerical solution from oscillating and smearing.

2.2. Stress model and material point method

The stress model for calculating the elasto-viscoplastic deformation of the solid assumes that the solid–liquid interface is sharp. In other words, the stress model is only solved in that region of the computational domain that is solid. The zero contour of the phase field is taken as the sharp solid–liquid interface and, hence, defines the boundary of the solid at any point in time. The solid–liquid interface is treated as stress free, since the stresses from the liquid are neglected. The development of a phase-field method that solves a unified equation of motion for the solid and liquid is beyond the scope of the present study. It is unclear how the mechanical property variations within the diffuse interface could be specified. Furthermore, the constitutive equations for the stresses would have to transition across the diffuse interface from those for an elasto-viscoplastic solid to those for a Newtonian fluid. These are important topics of future research.

The equation of motion for the solid is given by:

$$\rho \frac{d\boldsymbol{v}}{dt} = \nabla \cdot \boldsymbol{\sigma} + \rho \boldsymbol{b}, \tag{4}$$

where ρ is the density, $\boldsymbol{\sigma}$ is the Cauchy stress tensor and $\boldsymbol{b}$ is the gravity force vector. An elasto-viscoplastic constitutive model is used for the mechanical behavior of the solid, where the total strain, $\boldsymbol{\varepsilon}$, is decomposed into elastic, $\boldsymbol{\varepsilon}^e$, and viscoplastic, $\boldsymbol{\varepsilon}^{vp}$, parts (thermal strains are neglected). Two-dimensional plain-strain conditions are assumed. The elastic strains and stresses are related by Hooke's law. The elastic stiffness tensor is defined in terms of the Young's modulus, E, and the Poisson ratio, ν. For simplicity, a Perzyna-type model [19] is used for the viscoplastic material response. Hardening is neglected, i.e. the solid near the melting point is assumed to be perfectly viscoplastic. The viscoplastic strain rate is obtained from the J_2 associative flow rule:

$$\frac{d\boldsymbol{\varepsilon}^{vp}}{dt} = \gamma \frac{\partial f_Y}{\partial \boldsymbol{\sigma}}, \tag{5}$$

where γ is a consistency parameter defined as:

$$\gamma = \frac{\{f_Y\}}{\eta_{visc}}, \tag{6}$$

where η_{visc} is a viscosity coefficient and $\{\}$ are the Macaulay brackets [19]. The yield function, f_Y, is given by the standard von Mises yield criterion, in which σ_Y is the yield stress. The stress is integrated using the radial return mapping method [20].

The material point method [10] is used to solve the stress model. It originates from the particle-in-cell (PIC) method

[21] and takes advantage of both Eulerian and Lagrangian approaches. The solid is represented by a collection of Lagrangian material points, while the equation of motion is solved on fixed Eulerian background nodes (the same ones as used in the phase-field equation). The generalized interpolation material point method (GIMP) [22] is used to specify the mapping between the material points and the grid nodes. The mapping function is represented by the combination of a linear shape function, as in standard FEMs, and a Heaviside function, which specifies the support domain of each material point. The GIMP suppresses spurious oscillations when a material point passes through an Eulerian cell boundary. The details of the derivations and numerical implementation can be found in Refs. [22,23]. Since an explicit time integration scheme is used, the time step is small enough that the incremental strain can be assumed to be infinitesimal and the quadratic strain term is negligible. In order to maintain objectivity of the stress tensor under large deformation, the Jaumann stress rate is used.

For the newly solidified portion of a dendrite, new material points are inserted at the intersection of the zero phase-field contour with the fixed computational background mesh. These new material points are assigned zero initial stress and strain. This procedure is appropriate because it is assumed in the present study that the liquid does not transmit stresses to the solid. The mass of the new material points is chosen so as to match the amount of new solid for each cell from the phase-field computations.

2.3. Numerical tests and validation

2.3.1. Phase-field advection

The present implementation of the CIP method for the advection of the phase field is tested using the diagonal translation of a circle problem [17]. The advection part of the phase-field equation is solved by setting the right-hand side of Eq. (1) to zero. The square computational domain of side length 1.0, shown in Fig. 1a, is discretized using a 80×80 grid. Initially, a circle of radius 0.15 is placed at (0.25, 0.25). The circle is defined by the zero phase-field contour, and the phase field is initialized with the hyperbolic tangent profile $\phi = -\tanh(n/\sqrt{2}W)$, where n is the normal to the circle and $W = 2\Delta x$. The velocity field is uniform in the diagonal direction, advecting the circle to the (0.75, 0.75) position (half translation) and then back to the initial position (full translation).

Fig. 1c and d show the computed phase field when the circle is at the half and full translation positions, respectively. The initial, half translation and full translation zero phase-field contours are superimposed in Fig. 1b. It can be seen that the circular shape is well maintained during the translation. A grid convergence study showed that the order of accuracy of the CIP method for this problem is between 2.6 and 3.0. The nearly third-order accuracy is similar to the one for the CENO scheme used in Ref. [17].

2.3.2. Dendritic solidification with prescribed deformation

The phase-field model is first tested for dendritic solidification of a single crystal into an undercooled melt with prescribed deformation velocity fields for the solid (i.e. the stress model is not solved). Numerical tests are performed for both a rotational and a linear shear velocity field. Initially, a small solid seed is placed in the center of the computational domain, while the melt is uniformly undercooled. Symmetry conditions are imposed on the boundaries of the square computational domain. The domain is discretized using 641 node points in each direction with a uniform spacing of $\Delta x/W_0 = 0.4$. The dendritic solidification conditions are the same as in the second entry in Table 1 of Ref. [24]: a dimensionless initial melt undercooling of $\theta_i = -0.55$, a dimensionless thermal diffusivity of $D\tau_0/W_0^2 = 3$, a dimensionless capillary length of $d_0/W_0 = 0.185$, and an anisotropy strength of $\varepsilon = 0.05$. The reader is referred to Ref. [24] for all other details of the computations. It is shown in that reference that the present phase-field model, without flow and deformation, predicts steady dendrite tip growth velocities and radii that are in good agreement with the exact solution from microscopic solvability theory. Since the present phase-field model (with $\boldsymbol{v} = 0$) is the same as that in Ref. [24], the same agreement is obtained here. Fig. 2a provides a snapshot of the predicted phase field for the case of $\boldsymbol{v} = 0$. A typical 4-fold dendritic solidification pattern can be observed. Note that the actual computational domain is much larger than what is shown in Fig. 2.

In the first test case, a constant rotational velocity field is imposed over the entire computational domain, such that the dendrite rotates about its center as a rigid solid body. Since the melt is rotated at the same rate as the solid, the growth should be unaffected by the rotation. Fig. 2b shows the predicted phase field after a $\pi/4$ rotation. The rotational velocity was chosen such that after the $\pi/4$ rotation the dendrite has the same size as without rotation. No smearing of the phase field can be observed and the dendrite appears the same as without rotation. The zero phase-field contours with and without rotation are superimposed in Fig. 2d. In this figure, the dendrite of Fig. 2b is rotated back to the initial position. There is excellent agreement between the contours, indicating that the numerical treatment of the temperature, phase field and angle advection terms is satisfactory. The importance of accurately solving the crystallographic orientation angle evolution equation is illustrated in Fig. 2c. For that figure, Eq. (3) was not solved and the angle was kept at its original value at each location. An unrealistic "swirling" dendrite shape results.

In the second test case, a downward linear shear velocity field is imposed over the entire computational domain, as illustrated in Fig. 3a. The vertical velocity is zero at the origin of the dendrite and increases linearly in the horizontal direction. The velocity gradient is chosen such that the dendrite experiences significant bending during its growth (see Ref. [25] for details). Computed zero phase-field contours are shown for several intermediate times in Fig. 3b. The

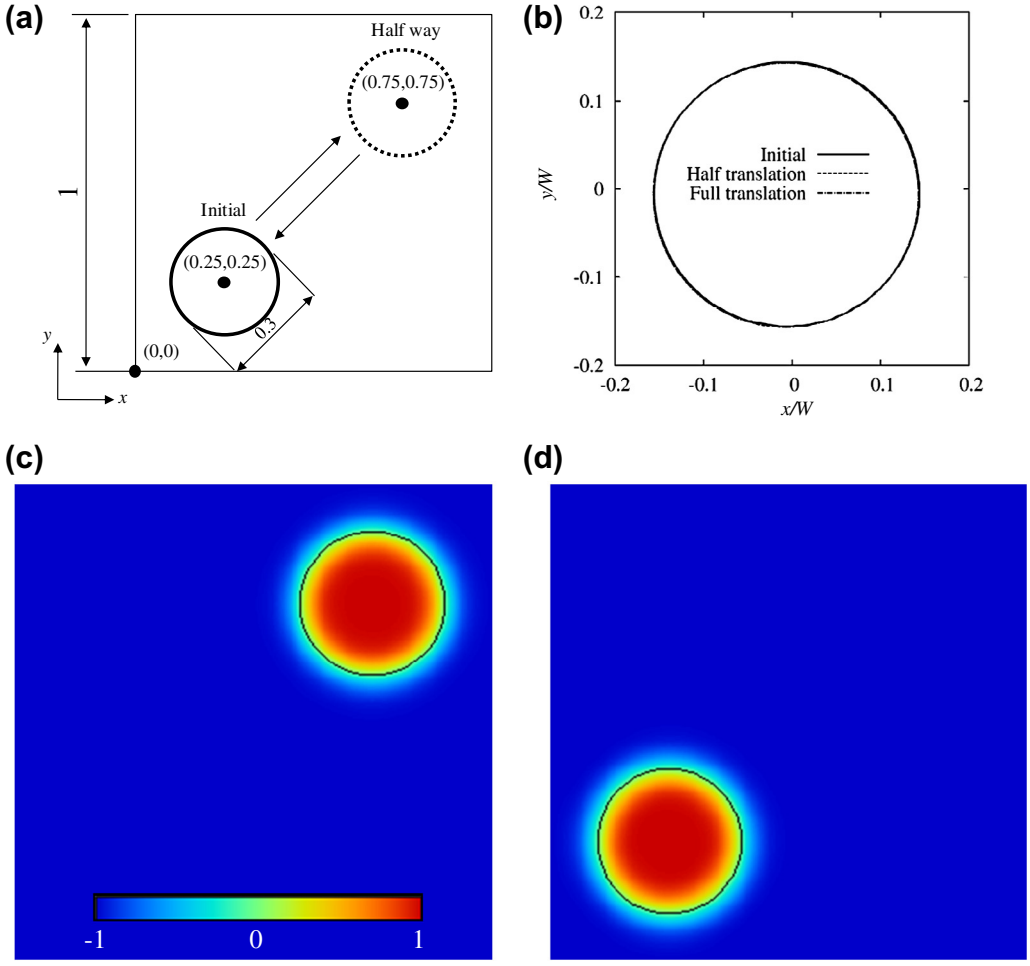

Fig. 1. Test of the high-order advection algorithm. (a) Schematic of the diagonal translation of a circle problem. (b) Calculated zero phase-field contours after half and full domain translation superimposed on the initial contour. Computed phase fields after half (c) and full (d) domain translation.

trajectory of the tip of the horizontally growing dendrite arm is indicated in Fig. 3b as a bold solid line. This trajectory is in close agreement with one obtained analytically by superimposing the dendrite tip growth velocity in the absence of deformation with the given linear shear velocity field [25]. This superposition assumes that the flow that is approximately normal to the growth direction does not affect the tip growth [24]. The good agreement in the tip trajectory demonstrates that non-uniform and continuously changing velocities and crystallographic orientation angles are effectively handled by the present computational method. Note that at the left vertical axis, the upward pointing dendrite arm grows faster than the downward growing arm. This can be attributed to the advection of heat by the velocity field in the liquid. It is shown in Ref. [24] that flow in the direction opposite to the dendrite tip growth direction results in an enhancement of the tip velocity.

2.3.3. Solid deformation without solidification

The present implementation of the material point method for the stress analysis is tested using several numerical examples that do not involve solidification.

The elastic part of the stress model is validated using the Timoshenko cantilever problem illustrated in Fig. 4 [26]. The left edge of the cantilever is fixed, and a vertical load of $P = 100$ N is imposed on the right edge. The length and height of the cantilever are given by $l = 8$ m and $h = 1$ m, respectively. The material properties are set to $E = 3 \times 10^7$ Pa, $v = 0.3$, and $\rho = 1000$ kg/m^3. As shown in the lower panel of Fig. 4, the cantilever is represented by 144 cells and 512 material points (2×2 points in each cell). The fixed background mesh extends well beyond the cantilever. Fig. 5 provides a comparison of the computed vertical displacement profile along the horizontal centerline with the analytical solution of Timoshenko [26]. Excellent agreement can be observed.

The elasto-viscoplastic computations are tested using the dogbone-like rectangular tension specimen of the dimensions shown in Fig. 6. The specimen is represented by 288 material points (2×2 points in each cell). First, the purely elastoplastic material response is examined by setting the viscosity coefficient, η_{visc}, to a very large number. A cyclic displacement profile is imposed at the top and bottom ends of the specimen, with maximum tension and compression strains of $\pm 0.5\%$. The same elastic prop-

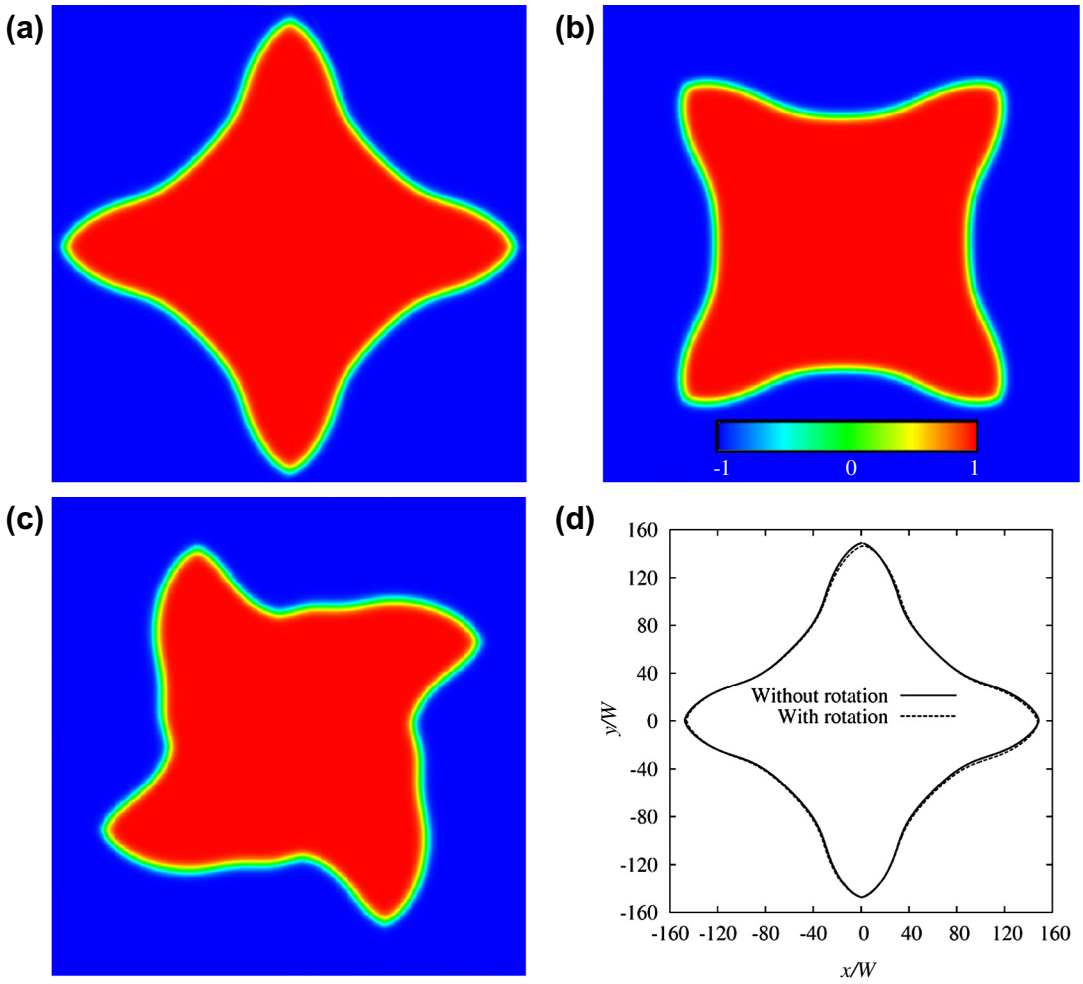

Fig. 2. Phase-field simulation of dendritic solidification with an imposed rotational velocity field. (a) Snapshot of the predicted phase field without rotation. (b) Calculated phase-field after a 45° revolution. (c) Swirling dendrite resulting from the lack of considering the crystallographic orientation angle changes in the phase-field equation. (d) Superimposed zero phase-field contours corresponding to (a) and (b).

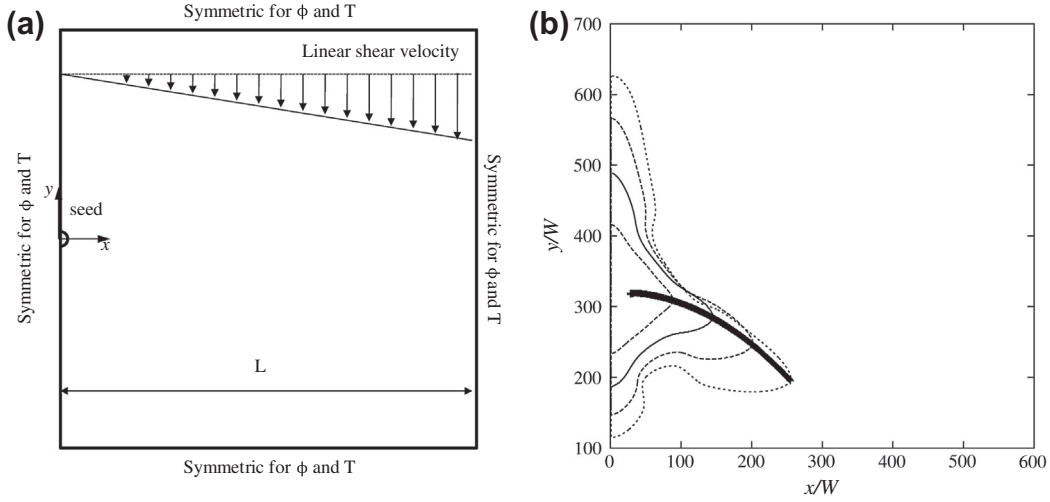

Fig. 3. Phase-field simulation of dendritic solidification under a linear shear velocity field. (a) Schematic of the computational domain and boundary conditions. (b) Predicted zero phase-field contours (every 5000 time steps) and dendrite tip trajectory.

erties as in the previous example are used, and the yield stress was set to $\sigma_Y = 6 \times 10^4$ Pa. Fig. 7a shows the computed stress–strain curve for one loading cycle. Yielding occurs exactly at the yield stress and the strains evolve as

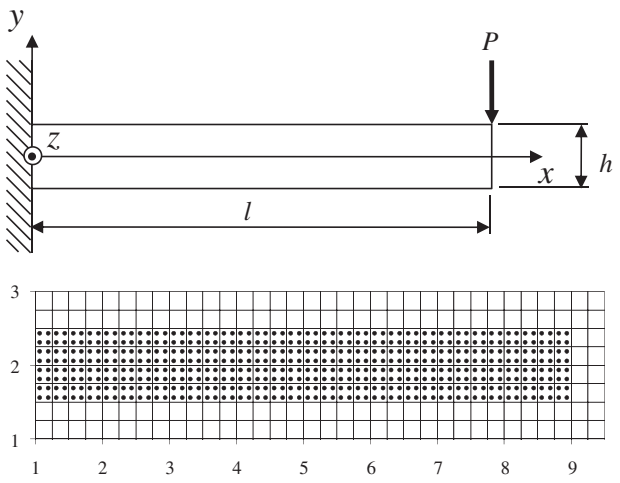

Fig. 4. Schematic of the Timoshenko cantilever problem (upper panel) and distribution of the Lagrangian material points on the fixed Eulerian background mesh (lower panel); the dimensions are in meters (i.e. $l = 8$ m and $h = 1$ m).

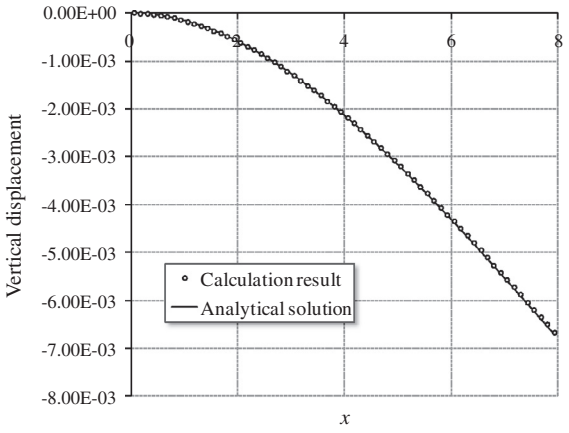

Fig. 5. Comparison of the predicted vertical displacement along the cantilever axis by the material point method with the analytical solution of Timoshenko (in meters).

expected. Second, the elasto-viscoplastic computations are tested for $\eta_{visc} = 3 \times 10^6$ Pa s. Simulations are performed for simple tensile loading of the specimen at three different strain rates. The resulting stress–strain curves are shown in Fig. 7(b). As expected, the yield stress increases with increasing strain rate. Oscillations in the calculated stresses are kept to a minimum.

The final test of the stress model is designed to examine the present implementation of the material point method for the case of large deformations. As illustrated in the left panel of Fig. 8, a rectangular bar ($L = 1$ m) is sheared by imposing equal rightward and leftward displacements at the top and bottom ends, respectively, such that the total shear is 40%. The solid is treated as a purely elastoplastic material with the same mechanical properties as in the previous example, except $\sigma_Y = 4 \times 10^8$ Pa. This test case also serves to check the advection of the phase field by the computed solid velocities. The initial representation of the bar by the phase field on the fixed background mesh is shown

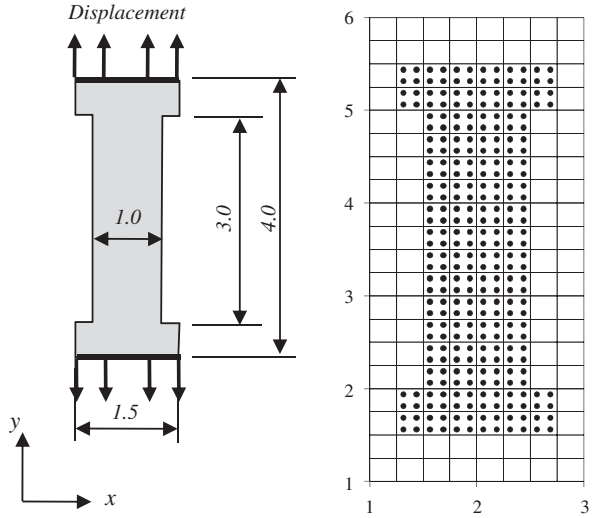

Fig. 6. Schematic of the specimen used in the tension–compression tests (left panel) and distribution of the Lagrangian material points on the fixed Eulerian background mesh (right panel); the dimensions are in meters.

in the right panel of Fig. 8. The background mesh is chosen to be five times as wide as the bar, in order to allow for the tracking of large lateral deformations. Computed von Mises stress (upper panels) and equivalent plastic strain (lower panels) contours for a shear of 40% are shown in Fig. 9. In this figure, the material point method results (left panels) are compared to standard FEM results (right panels) that were obtained using ANSYS 12.0 [27]. Overall, good agreement can be observed. The bar is predicted to yield everywhere except for a large complex-shaped central portion and small regions along the edges. The 40% shear represents the maximum that could be simulated using the FEM. Already, large amounts of finite-element mesh distortion and entanglement can be seen in the upper right and lower left corners of the bar. The material point method does not suffer from these problems. A more quantitative comparison of the material point method and FEM results is shown in Fig. 10. The computed von Mises stresses along the data sampling line indicated in the upper right panel of Fig. 9 are compared in Fig. 10a. While the agreement is qualitatively good, the material point method appears to better resolve the stress variations in the center of the bar. These stresses are very sensitive to the large deformations at the ends of the bar, where the FEM suffers from mesh entanglement. Fig. 10b shows a comparison of the deformed shape of the bar predicted by the FEM with the zero contour line of the phase field, which was advected using the solid velocity from the material point method stress analysis. The good agreement validates not only the material point method deformation calculations, but also the coupling with the phase-field advection algorithm.

3. Results and discussion

Simulations of the deformation of a single dendrite are performed using the physical system illustrated in Fig. 11

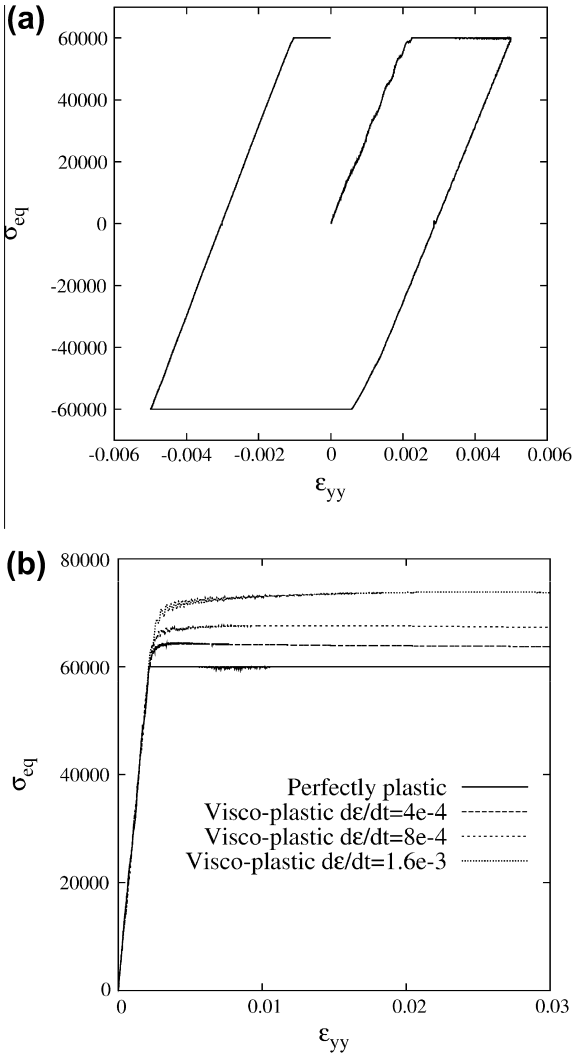

Fig. 7. Predicted stress–strain curves for the specimen of Fig. 6. (a) Fully reversed cyclic loading for an elastic–perfectly plastic solid. (b) Tension loading for an elastic–perfectly viscoplastic solid at three different strain rates.

. The rectangular domain is defined by 1200×800 grid points, with $\Delta x/W_0 = 0.4$, and is bounded by adiabatic walls. Initially, the domain contains an undercooled liquid, except for a solid seed at the center. The seed grows freely into the undercooled melt and develops into a dendrite. Unless otherwise noted, the dendritic growth conditions are the same as in the example of Section 2.3.2. Once the vertical dendrite arms reach the top and bottom walls, the walls start to move inwards at a prescribed rate. This imposes a compression loading on the growing dendrite. In order for some solidification to occur during the compression, the displacement rate of the top and bottom walls was chosen to be approximately equal to the dendrite tip growth velocity. This can be best observed in the figures below by the movement of the tips of the horizontally growing dendrite arms relative to the changes in the position of the top and bottom walls. Unless otherwise noted, the mechanical properties for the solid dendrite are taken as $E = 50$ GPa, $\nu = 0.33$, $\rho = 7800\ \mathrm{kg/m^3}$, $\sigma_Y = 5$ MPa and $\eta_{visc} = 1 \times 10^5\ \mathrm{Pa \cdot s}$. These values are intended to approximately represent the mechanical properties of metals near the melting point [3].

Before presenting the results of the simulations, it is necessary to explain the numerical treatment of the moving domain walls when solving the phase-field model. A special procedure is needed, because the numerical grid is fixed and does not deform. Hence, the moving domain walls cut through the computational cells at continuously changing positions. While the advection of the field variables by the motion of the solid is accounted for in the governing equations, it is important to accurately impose the boundary conditions at the moving domain walls. The cut-cell technique [28,29] is used for this purpose. Special boundary nodes are introduced and the equations are discretized using uneven node spacings. Special care is taken not to let the node spacings at the moving walls become smaller than half the node spacing of the fixed grid. The nodes behind the moving walls are deactivated. A validation test is presented in Ref. [25], where it is shown that the computed phase-field contours for a dendrite attached to a wall are indistinguishable for cases run with and without wall motion.

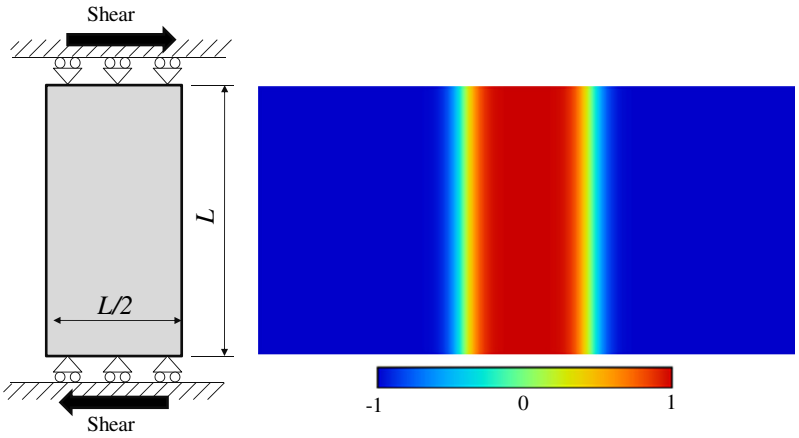

Fig. 8. Schematic of the specimen used in the large shear deformation test (left panel) and initial phase-field contours used to track the specimen boundary (right panel); $L = 50$ m.

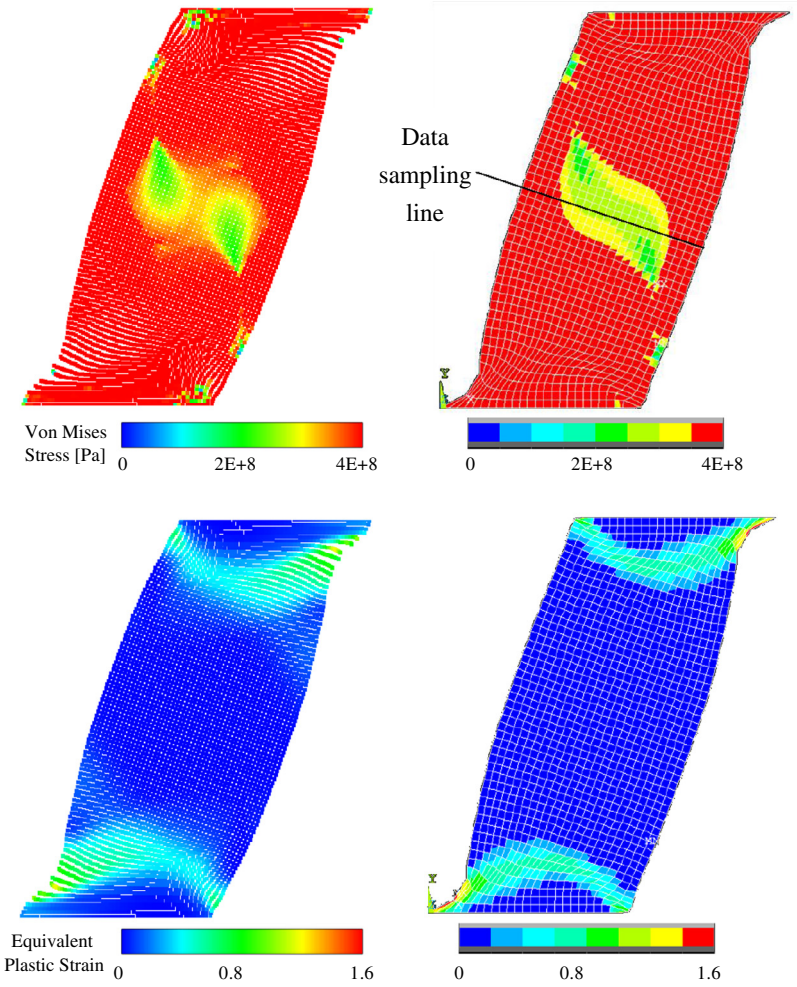

Fig. 9. Computed von Mises stress (upper panels) and equivalent plastic strain (lower panels) contours for the 40% shear deformation test of Fig. 8. The left panels are the results from the material point method, while the right panels are the results from the standard FEM code ANSYS 12.0.

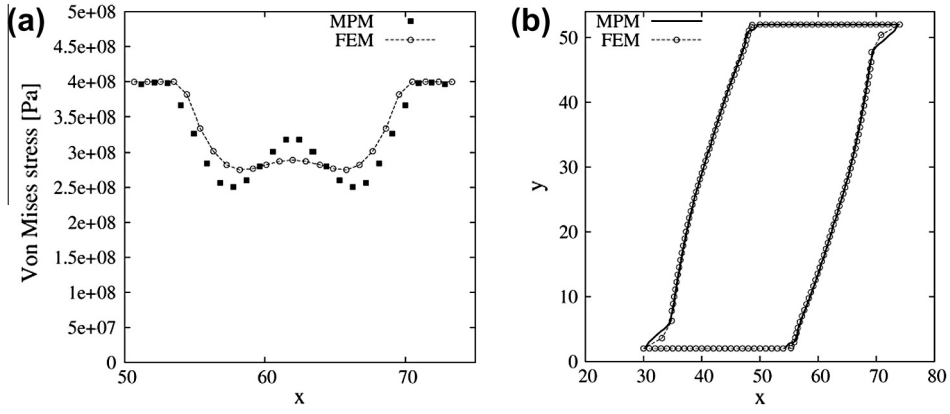

Fig. 10. Comparison of material point method and finite-element method results for the 40% shear deformation test of Fig. 8. (a) Predicted von Mises stresses along the data sampling line indicated in the upper right panel of Fig. 9. (b) Predicted specimen shapes.

The results of an initial simulation where the crystalline anisotropy strength is set to $\varepsilon = 0.015$ and viscous effects are neglected (i.e. $\eta_{visc} \to \infty$) are shown in Fig. 12. The rows of plots represent results at four different times corresponding to when the vertical dendrite arms have just touched the top and bottom walls, 5% compression, 10% compression and 15% compression. The phase-field contours (left column) and the equivalent plastic strain fields

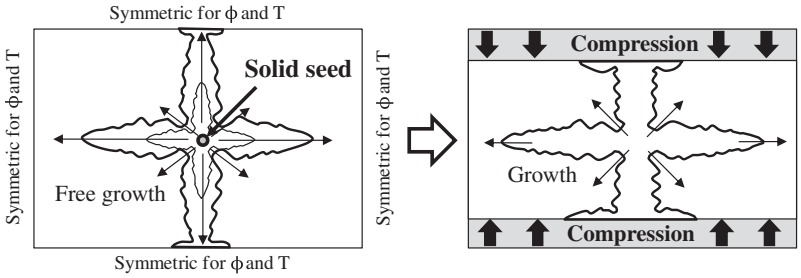

Fig. 11. Schematic of the computational set-up for the simulation of the compression of a single dendrite.

(center right column) indicate that the deformation of the dendrite for small compressive strains is limited to the vertical growing dendrite arms near the top and bottom moving walls. In these portions of the dendrite, the yield stress (center left column) is reached. As expected, the shape of the horizontally growing dendrite arms is unaffected by the compression. With increasing compression, the regions in the vertically growing dendrite arms that exhibit plastic deformation extend further towards the center of the dendrite. Furthermore, the (elastic) stresses in the center portion of the dendrite continually increase. However, due to the large cross-section of the dendrite in the center, the yield stress is not reached at 15% compression. There is also a thin layer of solid directly adjacent to the moving walls where the stresses are predicted to be below the yield stress. This can again be attributed to the larger cross-section of the dendrite at these locations. It is also interesting to observe the predicted evolution of the crystallographic orientation angle field in the rightmost column of Fig. 12. Bending of the dendrite occurs primarily in a thin layer at the edges of the regions with large plastic deformations, while the center portions of the vertically growing dendrite arms do not experience any crystallographic angle changes due to symmetry.

The deformation of a somewhat more complex dendrite structure is simulated next. For this purpose, a thermal noise term was introduced into the heat equation, Eq. (2), following exactly the procedure developed by Karma and Rappel [30] (see also Ref. [24]). The strength of the noise was chosen such that some side-branches develop during the growth of the dendrite. In addition, the anisotropy strength was increased to $\varepsilon = 0.06$ in order to obtain a

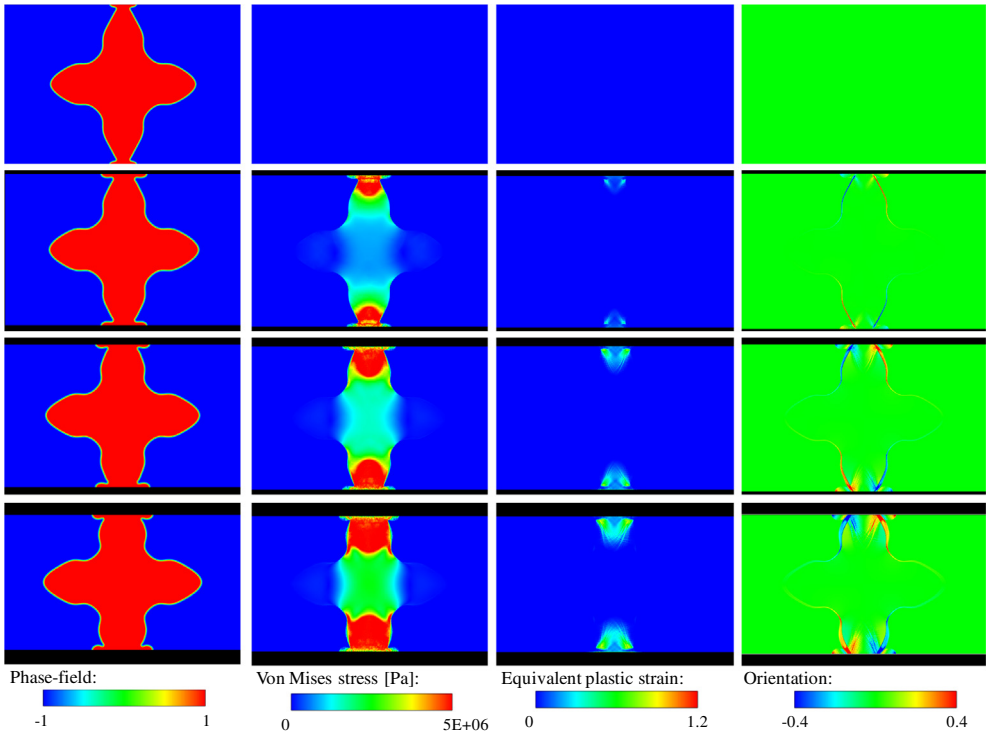

Fig. 12. Predicted phase-field (left column), von Mises stress (center left column), equivalent plastic strain (center right column) and crystallographic orientation angle (right column) contours for elastic – perfectly plastic compression of a single dendrite growing into an undercooled melt with an anisotropy strength of $\varepsilon = 0.015$ and no thermal noise (other conditions are provided in the text). Results are shown for when the vertically growing dendrite tips just touched the walls and compression is initiated (first row), at 5% compression (second row), at 10% compression (third row) and at 15% compression (fourth row).

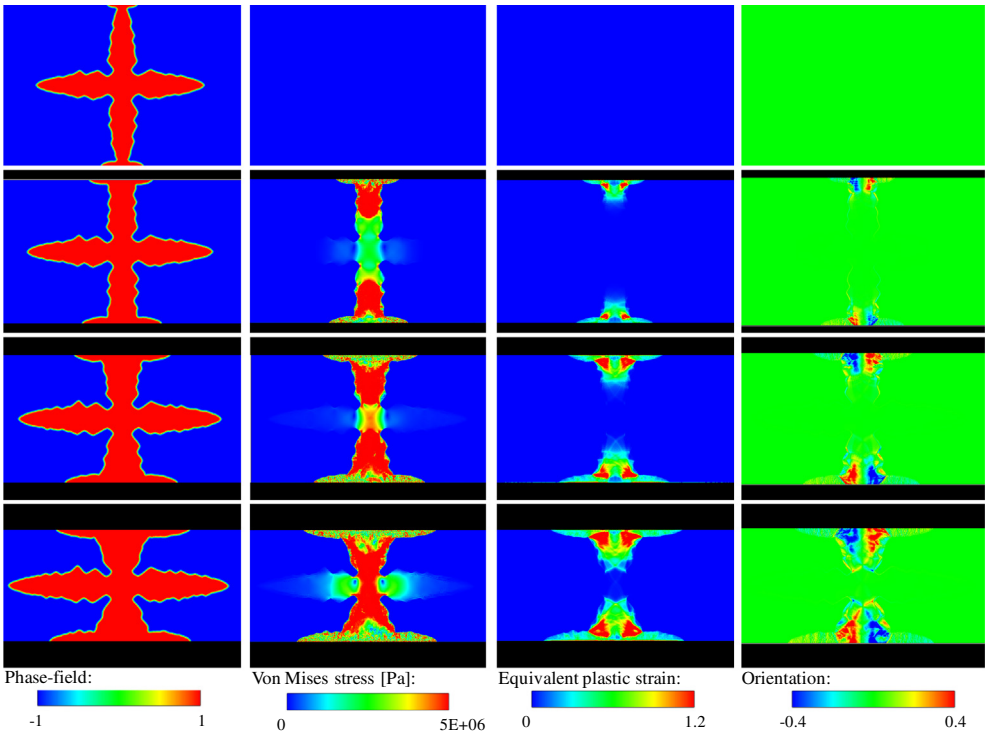

Fig. 13. Predicted phase-field (left column), von Mises stress (center left column), equivalent plastic strain (center right column) and crystallographic orientation angle (right column) contours for elastic–perfectly plastic compression of a single dendrite growing into an undercooled melt with an anisotropy strength of $\varepsilon = 0.06$ and thermal noise (other conditions are provided in the text). Results are shown for when the vertically growing dendrite tips just touched the walls and compression is initiated (first row), at 10% compression (second row), at 20% compression (third row) and at 30% compression (fourth row).

more slender dendrite. All other conditions are the same as those in the previous simulation (Fig. 12). Fig. 13 shows the computed results at compressions of 0%, 10%, 20%, and 30%. The phase-field contours in the upper left corner of Fig. 13 indicate that a more slender dendritic structure with small side-branches is indeed achieved. In particular, the necks between the center core and the four main dendrite arms are now much thinner. The stress, equivalent plastic strain and crystallographic orientation angle fields follow generally the same trends as in Fig. 12. Since the dendrite cross-section is much reduced, the plastic strains and orientation angle changes are much larger than in the previous simulation. Plastic strains in excess of 100% occur in portions of the dendrite near the moving walls. At 10% compression (second row in Fig. 13), small stress concentrations become apparent in the valleys between the side-branches and at the necks between the vertically growing arms and the dendrite core. Fig. 14 shows a close up of the predicted stress field in the center portion of the dendrite at 10% compression. It can be seen that in the narrow necks between the vertically growing arms and the dendrite core, small regions of solid very near the solid–

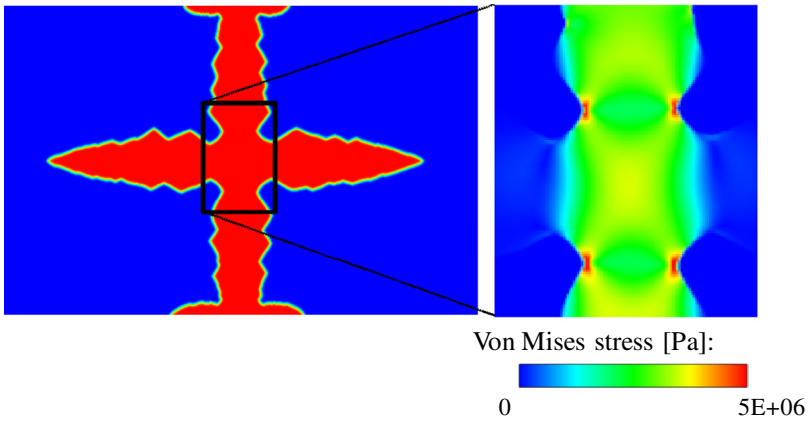

Fig. 14. Close-up image of the predicted phase-field (left panel) and von Mises stress (right panel) contours for the simulation of Fig. 13 at 10% compression.

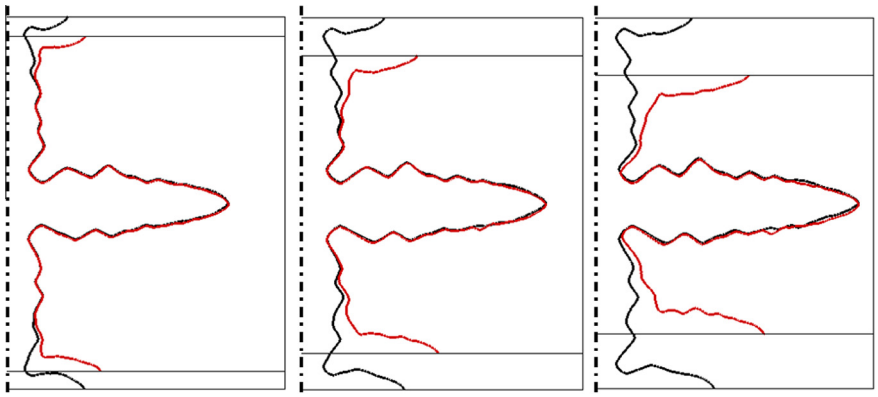

Fig. 15. Comparison of predicted zero phase-field contours with (red lines) and without (black lines) compression for the conditions of Fig. 13. Results are shown at times corresponding to 10% (left panel), 20% (center panel) and 30% (right panel) compression. Due to symmetry, only the right half of the computational domain is shown in each panel. (For interpretation of the references to color in this figure legend, the reader is referred to the web version of this article.)

liquid interface have already reached the yield stress (red), while the inner portions of the dendrite are still deforming elastically. At 20% compression (third row in Fig. 13), the center portion of the dendrite is starting to yield. At 30% compression (last row in Fig. 13), elastic stresses propagate even into the uncompressed horizontally growing dendrite arms. The large compression causes the vertically growing dendrite arms to appear much thicker than without compression. This can be better seen in Fig. 15, where the phase-field contours from two simulations with and without compression are directly compared at three different times. Due to the movement of the top and bottom walls, a large amount of solid mass is advected inwards.

Simulations were also performed where the viscous effect was included in the stress analysis [25]. The results are very similar to the ones in the previous example and are not included here for conciseness. Additional study of the rate dependency of the solid deformation is needed.

4. Conclusions

A method is developed to numerically simulate dendritic solidification with elasto-viscoplastic deformation of the solid. The phase-field method is used to model solidification, while the material point method is used to solve for the stresses and strains in the solid assuming a sharp and stress-free solid–liquid interface. Instead of modeling the flow in the liquid phase, the liquid velocity field is approximated through a zero-gradient extension of the solid velocities. Terms are added to the phase-field and heat equations to account for advection by the solid and liquid motion. Changes in the crystallographic orientation angle due to solid deformation are obtained from a separate evolution equation. The various parts of the model are carefully validated in several test cases. It is demonstrated that the chosen high-order numerical methods provide accurate results. The full model is then used to simulate the compression of a single dendrite. The results show that complex stress and strain distributions develop in the growing dendrite. The deformations result in variations in the crystallographic orientation angle within the dendrite that, in turn, affect the subsequent solidification behavior. The simulations demonstrate that the present numerical methodology is well suited for simulating large deformations of complex solidifying microstructures.

The simulations in this paper are limited to two dimensions and dendritic growth conditions that would be difficult to achieve in an experiment. These choices were made in order to achieve reasonable computational times (of the order of one day) on a standard single-processor computer workstation. More realistic, three-dimensional simulations would be needed to allow for an investigation into the constitutive behavior of semi-solid mushy zones in casting processes. Furthermore, the simulations in this paper are limited to deformation of a single dendrite without impingement of deformed dendrite arms on each other. In a companion paper [11], the present method is extended to consider multiple dendrites and the formation of grain boundaries. Future work should also include modeling of the flow of the liquid surrounding the deforming solid. In this respect, it would be desirable to solve a unified, phase-field dependent equation of motion for both the solid and the liquid. The main difficulty with such an equation would be to realistically model the transition from solid to liquid mechanical behavior inside of the diffuse interface. In the phase-field model of melt convection during solidification by Beckermann et al. [31], the solid was assumed to be rigid and stationary so that only a liquid momentum equation needed to be considered. Sun and Beckermann [32,33] extended this model to two immiscible Newtonian fluids having large property contrasts. A phase-field model for simultaneous solid deformation and liquid flow is still not available.

Acknowledgements

This work was financially supported, in part, by NASA under grant no. NNX10AV35G.

References

[1] Dantzig JA, Rappaz M. Solidification. Lausanne: EPFL Press; 2009.
[2] Flemings M. Metall Mater Trans B 1991;22:269.
[3] Pokorny MG, Monroe CA, Beckermann C, Zhen Z, Hort N. Metall Mater Trans A 2010;41:3196.
[4] Phillion AB, Cockcroft SL, Lee PD. Acta Mater 2008;56:4328.
[5] Fuloria D, Lee PD. Acta Mater 2009;57:5554.
[6] Uehara T, Fukui M, Ohno N. J Cryst Growth 2008;310:1331.
[7] Kobayashi R. Physica D 1993;63:410.
[8] Boettinger WJ, Warren JA, Beckermann C, Karma A. Ann Rev Mater Res 2002;32:163.
[9] Warren JA, Kobayashi R, Lobkovsky AE, Carter WC. Acta Mater 2003;51:6035.
[10] Sulsky D, Chen Z, Schreyer HL. Comput Methods Appl Mech Eng 1994;118:179.
[11] Yamaguchi M, Beckermann C. **Acta Mater** 2013;61:2268.
[12] Karma A, Rappel WJ. Phys Rev E 1998;57:4323.
[13] Gibou F, Fedkiw RP, Cheng L, Kang M. J Comput Phys 2002;176:205.
[14] Sun Y, Beckermann C. J Comput Phys 2007;220:626.
[15] Osher S, Fedkiw R. Level set methods and dynamic implicit surfaces. Heidelberg: Springer Verlag; 2003.
[16] Benson DJ. Comput Method Appl Mech 1992;99:235.
[17] Sokol Z. Q J R Meteorol Soc 1999;125:213.
[18] Takewaki H, Nishiguchi A, Yabe TJ. Comput Phys 1985;61:261.
[19] Simon JC, Hughes TJR. Computational inelasticity. Heidelberg: Springer Verlag; 1997.
[20] Krieg RD, Krieg DB. J Pressure Vessel Technol 1977;99:510.
[21] Harlow FH. Comput Phys Commun 1988;48:1.
[22] Bardenhagen SG, Kober EM. CMES 2004;5:477.
[23] Buzzi O, Pedroso DM, Giacomini A. CMES 2008;1:1.
[24] Tong X, Beckermann C, Karma A, Li Q. Phys Rev E 2001;63:061601.
[25] Yamaguchi M. PhD thesis, University of Iowa, Iowa City, IA; 2011.
[26] Timoshenko SP, Goodier JN. Theory of elasticity. 3rd ed. New York: McGraw-Hill; 1970.
[27] ANSYS 12.0. Basic Analysis Guide. Canonsburg, PA: ANSYS Inc.; 2009.
[28] Ingram DM, Causon DM, Mingham CG. Math Comput Simulat 2003;61:561.
[29] Ferziger JH, Peric M. Computational methods for fluid mechanics. 3rd edn. Heidelberg: Springer Verlag; 2002.
[30] Karma A, Rappel WJ. Phys Rev E 1999;60:3614.
[31] Beckermann C, Diepers HJ, Steinbach I, Karma A, Tong X. J Comput Phys 1999;154:468.
[32] Sun Y, Beckermann C. Physica D 2004;198:281.
[33] Sun Y, Beckermann C. Physica D 2008;237:3089.